metals

MDPI

Article

Microstructure and Mechanical Characterization of AISI 4340 Steel Additively Manufactured by Laser Powder Bed Fusion

Felix Aguilar [1], Thinh Huynh [1], Nemanja Kljestan [2], Marko Knezevic [2] and Yongho Sohn [1,*]

[1] Department of Materials Science and Engineering, University of Central Florida, Orlando, FL 32816, USA; felix.aguilar@ucf.edu (F.A.); thinh.huynh@ucf.edu (T.H.)
[2] Department of Mechanical Engineering, University of New Hampshire, Durham, NH 03824, USA; nemanja.kljestan@unh.edu (N.K.); marko.knezevic@unh.edu (M.K.)
* Correspondence: ysohn@ucf.edu

Abstract: The effects of laser powder bed fusion (LPBF) parameters, such as power (200 to 350 W) and scan speeds (from 200 to 2000 mm/s), on the microstructure and mechanical properties of high-strength, low-alloy (HSLA) AISI 4340 steel were examined. A wide range of volumetric energy density (VED) between 93 and 162 J/mm^3 produced samples with relative densities greater than 99.8%. The optimal parameter set was identified with laser power = 200 W, scan speed = 600 mm/s, hatch spacing = 0.12 mm, and slice thickness = 0.03, corresponding to VED = 92.6 J/mm^3. Scanning electron microscopy revealed a predominantly martensitic microstructure for all processing parameters examined, although X-ray diffraction revealed the minor presence of retained austenite within the as-fabricated 4340 steel. Using the optimized LPBF parameters, the as-fabricated 4340 steel exhibited a yield strength of 1317 MPa ± 16 MPa, ultimate tensile strength of 1538 MPa ± 22 MPa, and 18.6 ± 1% strain at failure. These are similar to wrought 4340 steel quenched and tempered between 400 and 600 °C.

Keywords: laser powder bed fusion; high-strength steels; AISI 4340; mechanical properties; microstructure; martensite

Academic Editors: Paul Wood and Urvashi Fowdar Gunputh

Received: 25 February 2025
Revised: 31 March 2025
Accepted: 2 April 2025
Published: 5 April 2025

Citation: Aguilar, F.; Huynh, T.; Kljestan, N.; Knezevic, M.; Sohn, Y. Microstructure and Mechanical Characterization of AISI 4340 Steel Additively Manufactured by Laser Powder Bed Fusion. *Metals* **2025**, *15*, 412. https://doi.org/10.3390/met15040412

1. Introduction

Laser powder bed fusion (LPBF) is a common additive manufacturing (AM) process for the production of dense, near-net-shape engineering components with complex geometries using metallic alloys. The LPBF process utilizes a high-power laser to melt a selected region of a metal powder bed, which is then rapidly solidified at rates between 10^3 and 10^8 K/s, building the component layer by layer based on a computer-generated model [1–3]. AISI 4340 grade steel is a heat-treatable, nickel–chromium–molybdenum, high-strength, low-alloy steel. It is conventionally employed in quenched and tempered conditions, where tempering is carried out to tailor the mechanical properties to different applications by enhancing the ductility and toughness of the martensitic as-quenched 4340 steel. Due to its high wear resistance, strength, and toughness, AISI 4340 steel has been utilized in numerous high-performance applications in aerospace, automotive, and military industries in the form of axles, shafts, and transmission gears [4–8].

Given the intense interest in additive manufacturing of metallic alloys, studies have been conducted to examine the effects of various LPBF parameters on many different alloy systems with the intent of optimizing the relative density and mechanical properties of as-fabricated components. In general, the relative density, microstructural, and mechanical properties of an alloy processed through LPBF are most influenced by the laser power (P),

laser scan speed (v), hatch spacing (h), and slice thickness (t) [9–11]. The volumetric energy density (VED) has been widely used to simplify the comparison between alloy samples produced across varying LPBF parameters. VED is determined using the relation [1,2]:

$$VED = \frac{P}{v \times h \times t} \quad (1)$$

Previous studies [4,5,7–9,12–14] have evaluated the LPBF processing of AISI 4340 steel and reported that sample densities greater than 99.8% were observed at an energy density within the range of 100–140 J/mm^3. The as-fabricated 4340 steel was found to exhibit mechanical properties similar to wrought 4340 steel. Additionally, the as-fabricated 4340 steel in these studies was found to exhibit a predominant martensitic microstructure.

Yao et al. [7] reported excellent compatibility of 4340 with AM processing, with the presence of bainite, and discussed tuning the AM parameters to achieve optimal strength–ductility–toughness considerations. Ryder et al. [12] conducted a comprehensive analysis of the melt pool dimensions as functions of the LPBF parameters for 4340 steel and developed a computational prediction model for the melt pool depth, width, and morphology as a function of scanning speed and laser power. They proposed that fine cellular substructures found in the as-fabricated matrix contributed to the strengthening of 4340 steel produced by LPBF. Hearn et al. [13] investigated the effects of build plate pre-heat temperature on the relative density and mechanical properties of as-fabricated 4340 steel and reported that relatively high build plate pre-heat temperatures of 100 to 175 °C could improve the relative density. Furthermore, it was also reported that the high substrate temperature could mitigate the formation of cracks during the LPBF process by reducing the residual stress of the as-fabricated 4340 steel. Jellis et al. [14] evaluated the effects of build orientation on the mechanical properties of as-fabricated 4340 steel. They reported an increase in elongation for as-fabricated tensile bars built with their length parallel to the build direction. However, they also reported that this orientation caused an increase in the hardness gradient between the top and bottom of the tensile bars.

This study aims to further document the LPBF printability and mechanical properties of as-fabricated 4340 steel by a detailed examination on the influence of different LPBF parameters on the microstructure and phase constituents of 4340 steel. The influence of LPBF parameters on the relative density, microstructure, phase constituent development, and mechanical properties is reported in this study. The results reported in this work contribute to an additional understanding of the influence of LPBF parameters on the microstructure and properties of LPBF-processed 4340 steel.

2. Materials and Methods

2.1. Laser Powder Bed Fusion and Specimen Preparation

Commercially available gas-atomized AISI 4340 steel powder feedstock used in this study was obtained from GKN Powder Metallurgy (Cinnaminson, NJ, USA). The chemical composition of the as-received powders was, in wt.%, 1.96 Ni, 0.28 Si, 0.88 Cr, 0.79 Mn, 0.06 Cu, 0.26 Mo, 0.41 C, and 95.36 Fe. Prior to LPBF, the particle size distribution was determined using a Beckman-Coulter (Beckman Coulter, Inc., Brea, CA, USA) LS 13 320 laser diffraction particle size analyzer. An SLM 125^{HL} (SLM Solutions Group AG, Lübeck, Germany) LPBF system, equipped with a single continuous-wave IPG Yb-fiber laser with a beam spot size and wavelength of approximately 70 µm and 1070 nm, respectively, was employed to print cubic samples with dimensions of 10 mm × 10 mm × 10 mm using varying combinations of laser power and scan speed, as listed in Table 1. In this study, the slice thickness and hatch spacing were held constant at 0.03 mm and 0.12 mm, respectively. The build plate was pre-heated to 100 °C, and ultra-high-purity Ar gas was used to maintain

an inert atmosphere with an oxygen concentration below 0.2%. Surface finish scanning strategies, such as contouring, up-skin, and re-melting, were not implemented in order to focus on understanding the correlation between laser power and scan speed on the relative density and microstructure of the samples.

Table 1. LPBF parameters examined in this study for 4340 steel.

Power (W)	Speed (mm/s)	Slice Thickness (mm)	Hatch Spacing (mm)	Scan Rotation (°)	Energy Density (J/mm^3)	Relative Density (%)
200	200	0.03	0.12	67	278	97.70 ± 2.35
	400				139	99.78 ± 0.12
	600				92.6	99.89 ± 0.09
	800				69.4	98.79 ± 0.57
	1000				55.6	94.32 ± 1.37
	1200				46.3	91.00 ± 2.22
	1400				39.7	83.90 ± 3.06
350	600				162	99.99 ± 0.01
	800				122	99.94 ± 0.03
	1000				97.2	99.90 ± 0.06
	1200				81.0	99.56 ± 0.29
	1400				69.4	98.94 ± 0.35
	1600				60.8	97.59 ± 0.77
	1800				54.0	95.73 ± 1.58
	2000				48.6	89.58 ± 1.32

After LPBF processing, the cubes were removed from the build plate without stress-relieving treatments and sectioned using a slow-speed diamond saw, both parallel (XZ) and perpendicular (XY) to the build direction. The samples were cold-mounted in epoxy, metallographically ground using SiC, and polished to a 0.05 µm finish with colloidal silica suspension. Prior to etching, five micrographs were taken at 100× magnification on each sample for the XZ and XY cross-sections using a Nikon Metaphot (Nikon Metrology Inc., Tokyo, Japan) optical microscope at random locations. ImageJ (National Institutes of Health, Bethesda, MD, USA) image analysis version 1.54j software was employed to quantitatively measure the relative density in each sample from both XZ and XY directions.

2.2. Phase Constituent and Microstructure Analysis

X-ray diffraction (XRD) was carried out using a Panalytical Empyrean X-ray diffractometer (Malvern Panalytical, Westborough, MA, USA) equipped with Cu K_α radiation source. The XRD patterns were collected at 45 kV and 40 mA, with scanning angles ranging from 30° to 100° and from 40° to 50° 2θ, using a step size of 0.03° with dwell times of 90 and 300 s, respectively. A β-Nickel filter was used to improve the noise-to-background ratio due to fluorescent effects. All XRD patterns were analyzed using the Panalytical HighScore Plus (Malvern Panalytical, Westborough, MA, USA) version 4.5 software. Selected samples were etched with 2% Nital for approximately 2 to 3 s for microstructural analysis, which was carried out using a Zeiss^{TM} Ultra-55 (Carl Zeiss AG, Jena, Germany) field emission scanning electron microscope (FE-SEM) operating at 20 kV.

2.3. Mechanical Testing

Vickers hardness measurements were carried out using a LECO™ LV700 (LECO Corporation, St. Joseph, MI, USA) hardness indenter to examine the relationship between processing parameters and microstructure of the as-printed alloy. Nine microhardness measurements were carried out for each sample consisting of a 10 kgf load, with a dwell time of 10 s. Indentations were performed on each of the selected samples as shown in Figure 1.

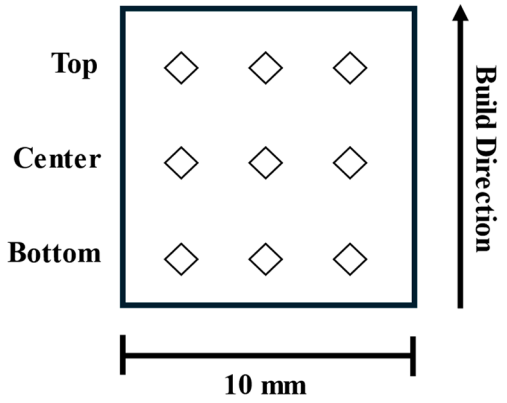

Figure 1. Schematic of Vickers hardness indentation locations on the cross-section of as-fabricated LPBF 4340 steel.

To determine the tensile properties of the as-fabricated AISI 4340 steel, three dog-bone-shaped tensile bars were built with the optimized parameters determined in this study (200 W and 600 mm/s). The geometry of the tensile bars was in accordance with ASTM E8/E8M [15] standard consisting of a gauge length of 25 mm and gauge cross-sections of 6 mm × 10 mm. The bars were built parallel to the build plate surface as shown in Figure 2b and removed from the build plate without residual stress relieving treatment. The sides of the tensile bars were ground to 1200 grit finish using SiC. Tensile testing was carried out using a MTS^{TM} Landmark 370 (MTS Systems Corporation, Eden Prairie, MN USA) instrument at a quasi-static strain rate of 10^{-4} s^{-1} measured using a 25 mm extensometer.

Figure 2. (**a**) Top view and (**b**) cross-sectional view of the grip section of the tensile specimens used in this study.

3. Results

3.1. Powder Feedstock

Figure 3 presents the particle size distribution of the as-received powder feedstock. The particle sizes, including D10, D50, D90, and the mean particle size, were 51.62, 74.76, 116.29, and 74.76 µm, respectively. The secondary electron micrograph presented in Figure 4a shows that the morphology of the powders was spherical, with a small amount of satellites on the powder surface. The cross-sectional backscatter electron (BSE) micrograph in Figure 4b highlights the martensitic microstructure of the AISI 4340 steel powders decorated with a segregate cell structure.

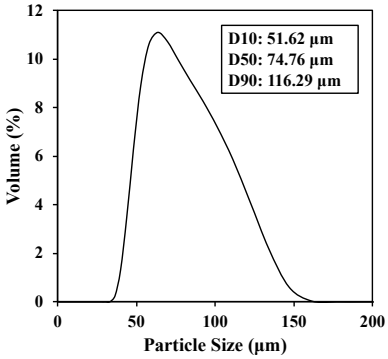

Figure 3. Particle size distribution of AISI 4340 steel powders.

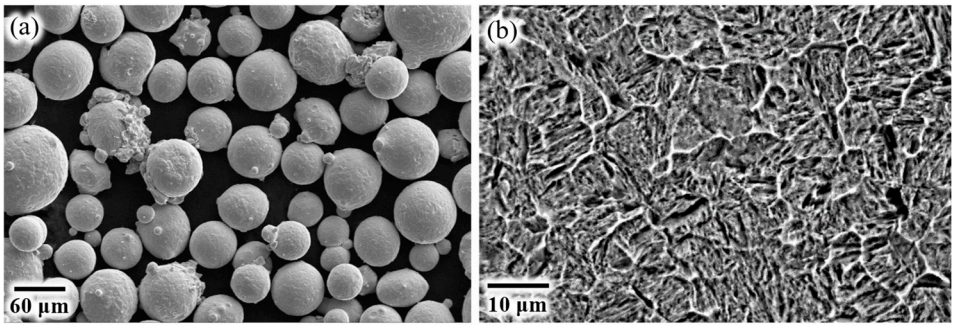

Figure 4. (**a**) Secondary electron micrograph and (**b**) cross-sectional backscatter electron micrograph of AISI 4340 steel powders.

3.2. Influence of LPBF Parameters on Relative Density

Figure 5 presents representative cross-sectional optical micrographs of the samples examined as a function of LPBF parameters. Dark features correspond to porosity and/or flaws. No solidification or cold cracking was observed in any of the LPBF samples investigated in this study. The samples outlined by the dotted line in Figure 5 had relative densities greater than 99.8%. These samples were produced using volumetric energy densities ranging from 93 to 162 J/mm^3, which is consistent with values reported in the literature [7,11–14]. In general, samples produced with high volumetric energy density, i.e., high laser power and/or low scan speed, yielded highly circular porosities, typically referred to as keyhole pores [1–3]. In contrast, samples produced using lower energy density yielded irregularly shaped flaws, typically known as lack-of-fusion flaws [1–3], which increased in number and size with decreasing volumetric energy density.

Figure 6a,b present the relative density of the as-fabricated samples as a function of laser scan speed using laser powers of 200 and 350 W. For samples produced using 200 W, the relative density increased with increasing scan speed, then remained above 99.8% between 400 and 800 mm/s before decreasing. Samples produced using 350 W had relative densities above 99.8% at the lower scan speeds and then decreased at scan speeds greater than 1200 mm/s. Generally, no significant variation in relative density was observed between the XZ and XY cross-sections, with the exception of the sample fabricated using 350 W and 1800 mm/s, which also exhibited a large standard deviation due to low relative density. Similar results can be obtained by examining the relationship between the VED and sample relative density. As shown in Figure 6c, the density of the samples increased sharply until reaching ~99.8% at VED of approximately ~93 J/mm^3 and then decreased once VED was greater than 162 J/mm^3. The optimal laser power and scanning speed parameters chosen to be reported in this study were 200 W and 600 mm/s, respectively, yielding a relative density of 99.9%.

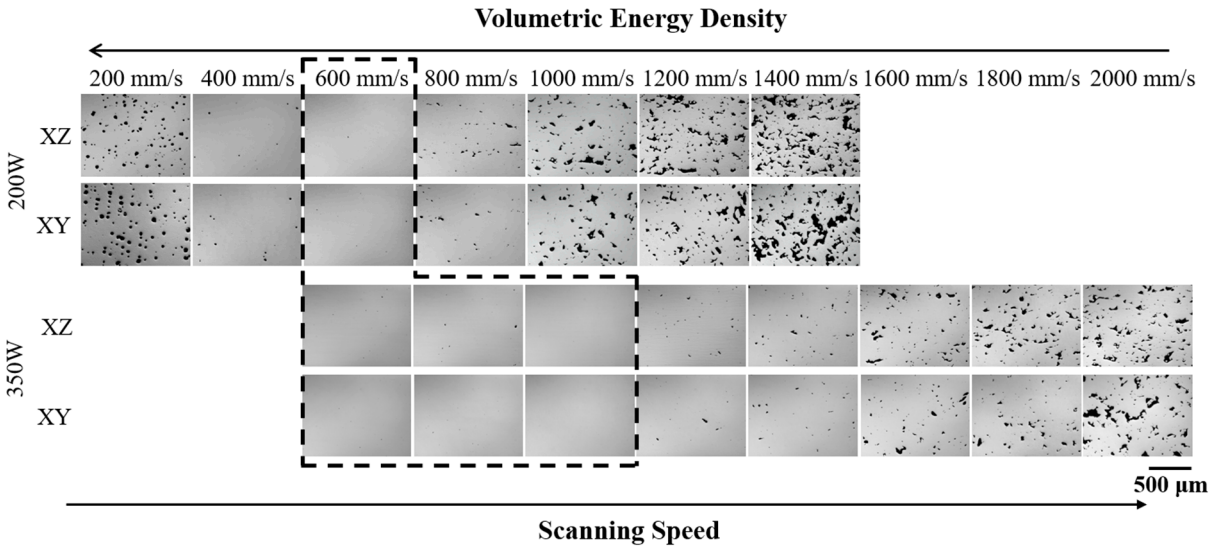

Figure 5. Optical micrographs of the XZ and XY cross-sections from the LPBF AISI 4340 steel produced using various laser powers and scan speeds. Samples highlighted with dashed line box exhibited average relative densities greater than 99.80%.

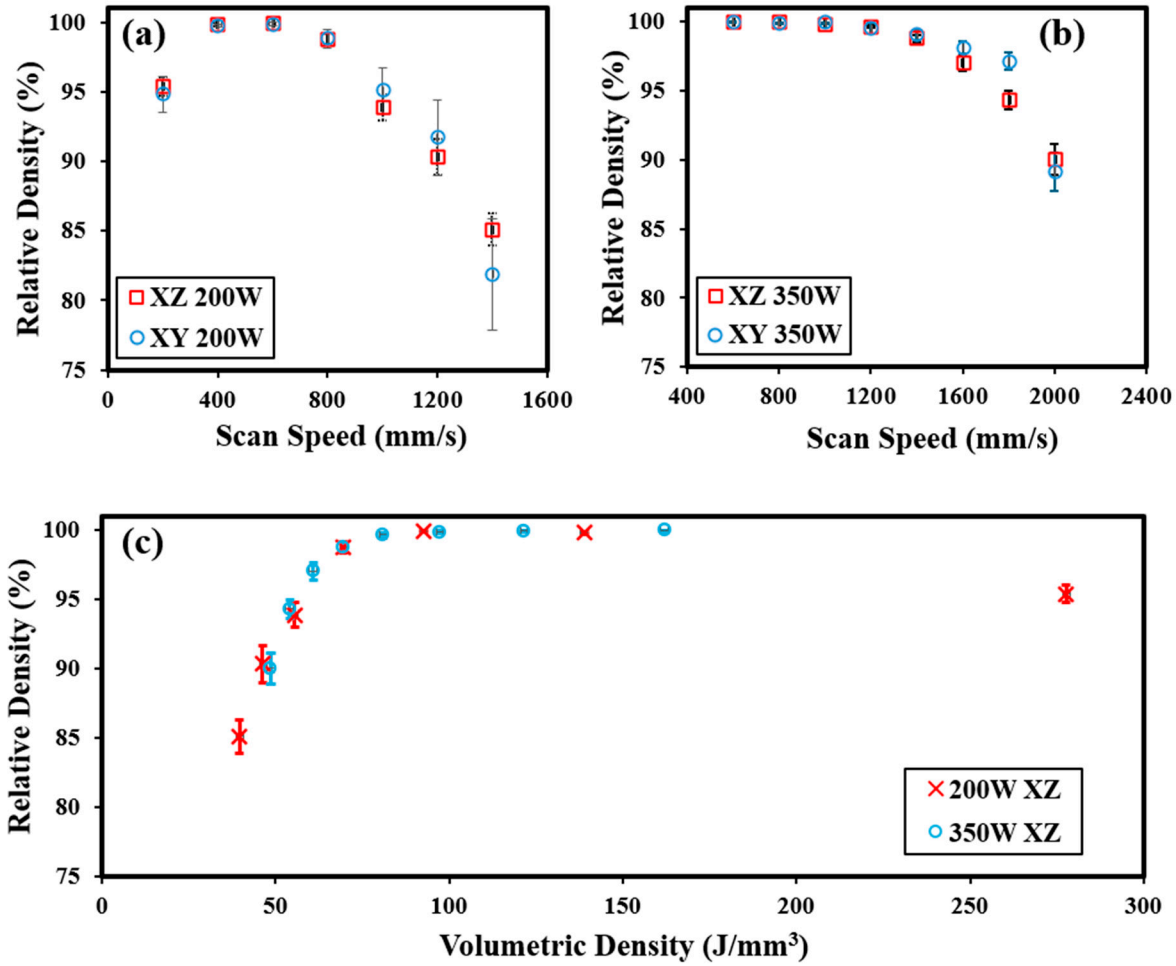

Figure 6. Relative density of LPBF samples as a function of scan speed using laser powers of (**a**) 200 W and (**b**) 350 W. (**c**) Relative density of LPBF samples as a function of volumetric energy density.

3.3. Influence of Processing Parameters on Microstructure

Figure 7a presents the XRD patterns for samples produced using various laser scan speeds and powers. The diffraction peaks located at 44.6°, 64.8°, 82°, and 98.6° correspond to the α′ martensite phase. Figure 7b presents a clear appearance of a weak diffraction peak at 43.5°, which was observed for all LPBF parameters examined, except for the sample produced using 200 W and 200 mm/s. This low-intensity peak is likely associated with the (111) from retained austenite or the (102) Fe_3C. Retained austenite has been reported in wrought quenched 4340 steels by Sastry and Wood [16], as well as in LPBF 4340 steel [7] and many other LPBF steels [17]. On the other hand, Fastow et al. [18] examined the laser surface-melted 4340 steel and reported that the microstructure in the melt pool consisted mainly of martensite, with no retained austenite present. A thorough microstructural examination through SEM could not confirm the presence of retained austenite or cementite in the as-printed samples. Detailed XRD patterns for the appearance of (111) from the retained austenite phase are presented in Figure 8.

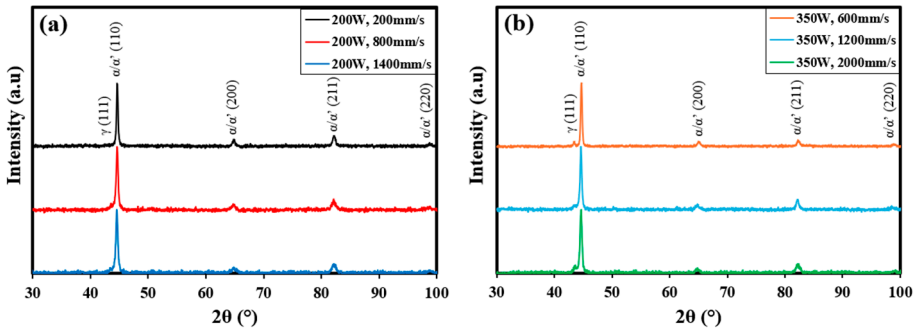

Figure 7. XRD patterns of LPBF AISI 4340 steel produced using various laser scan speeds at laser power of (**a**) 200 W and (**b**) 350 W.

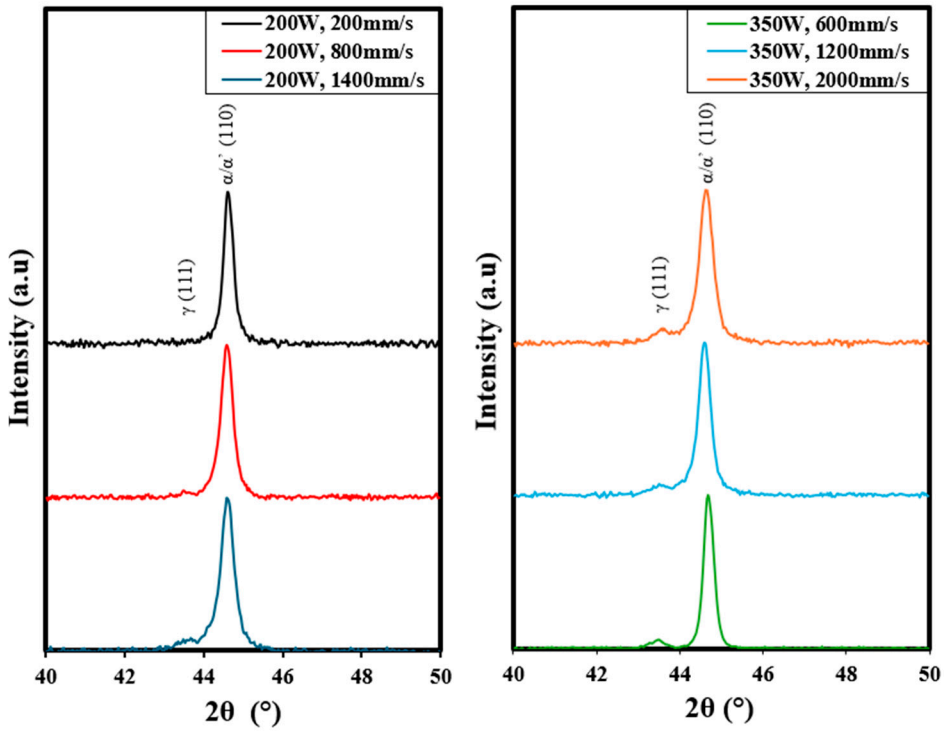

Figure 8. XRD patterns from 40° to 50° 2θ of selected LPBF AISI 4340 steel samples.

Table 2 and Figure 9 present the volume fractions of the retained austenite phase present in the LPBF 4340 steel, estimated using the following equations [19]:

$$V_\gamma + V_{\alpha'} = 1 \quad (2)$$

$$V_\gamma = \frac{1.4I_\gamma}{I_{\alpha'} + 1.4I_\gamma} \quad (3)$$

where V_γ and $V_{\alpha'}$ are the volume fractions of austenite and martensite, respectively, I_γ and $I_{\alpha'}$, and are the integrated intensities of (111) and (110) peaks from the austenite and martensite, respectively. Plotting the austenite volume fraction as a function of volumetric energy density reveals that there is a decrease in the volume of retained austenite with increasing volumetric energy densities. Note that the volume fraction of retained austenite for the sample printed using 278 J/mm^3 is estimated to be zero, since no austenite diffraction peak was identified from the XRD.

Table 2. Volume fraction of austenite present in as-fabricated 4340 steel.

Power (W)	Speed (mm/s)	Energy Density (J/mm^3)	Volume Fraction
200	200	278	0
	800	69.4	0.135
	1400	39.7	0.112
350	600	162	0.0901
	1200	81	0.110
	2000	48.6	0.167

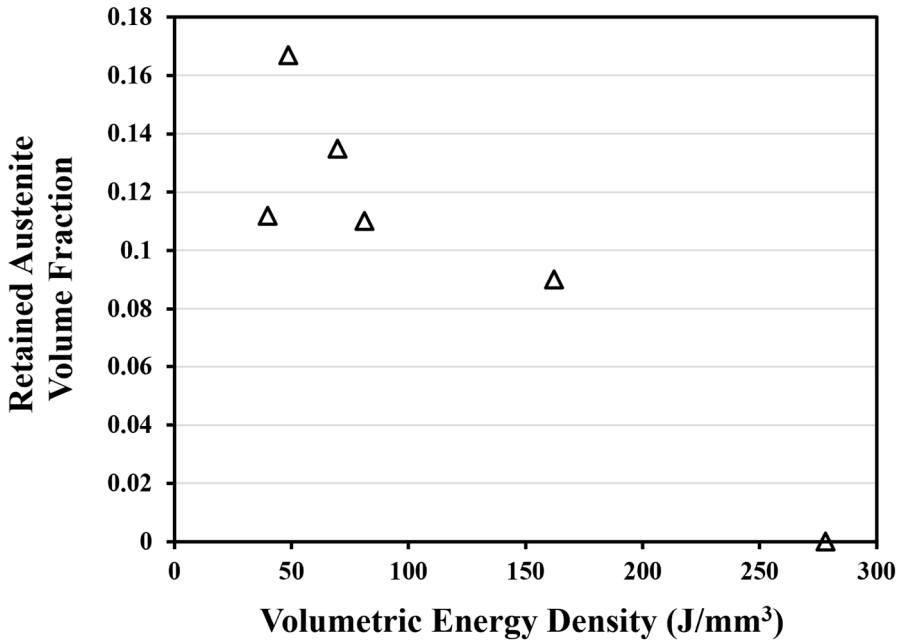

Figure 9. Volume fraction of retained austenite as a function of volumetric energy density for as-fabricated 4340 steel.

Figure 10 presents the BSE micrographs of samples produced using 200 W and various scan speeds. The as-fabricated 4340 steel was primarily martensitic and decorated with cellular segregation, likely containing alloying elements such as Cr, Mo, and Ni [20,21]. As

shown by the BSE micrograph in Figure 11, the as-fabricated 4340 steel exhibited an alternating pattern of fine martensite within the melt pools and coarse martensite laths along the melt pool boundaries and heat affected zones surrounding the melt pool boundaries. This is similar to what has been reported in other martensitic steels where the presence of coarse martensite regions has been attributed to regions that were exposed to austenitization temperatures during the deposition of a new layer on top [21,22]. No significant microstructural deviation from this alternating pattern of coarse and fine martensite regions was observed along the build direction or between samples processed at different scan speeds.

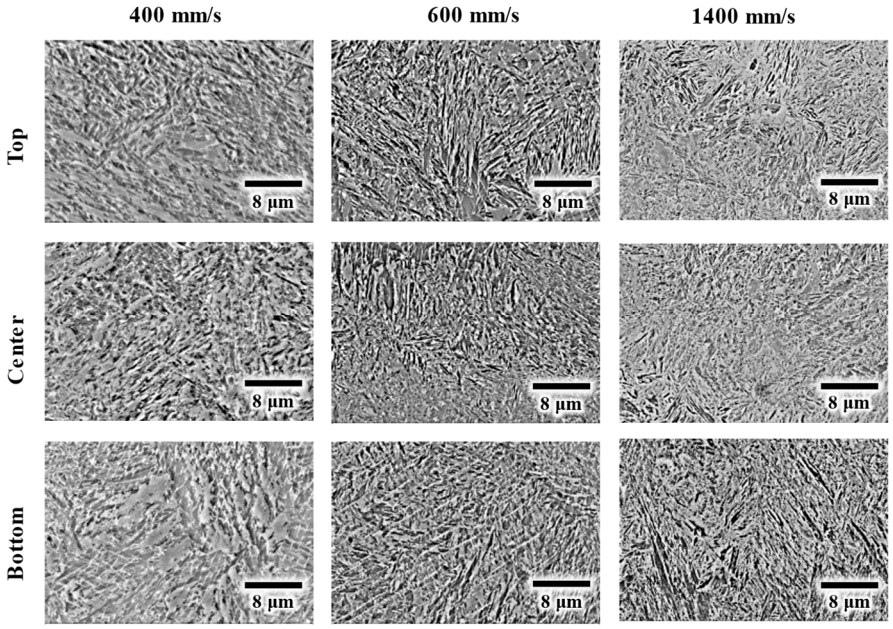

Figure 10. Backscatter electron micrographs of as-fabricated AISI 4340 cubes, produced using a laser power of 200 W, as a function of scanning speeds and build height.

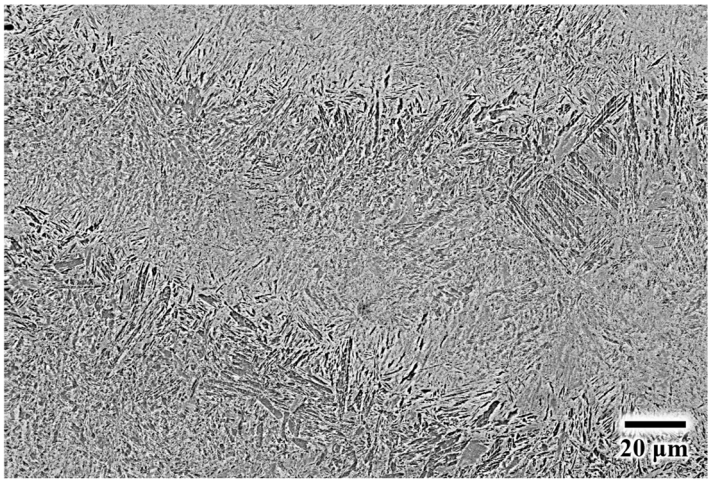

Figure 11. Backscatter electron micrograph of typical alternating fine and coarse martensite layers in as-fabricated 4340 steel.

3.4. Influence of Processing Parameters on Mechanical Performance

Figure 12 presents the Vickers hardness of select as-fabricated AISI 4340 steel cubes as a function of volumetric energy density. This plot demonstrates that the hardness exhibited by the as-fabricated samples generally decreased with increasing VED values, which agrees with the trend reported by Yao et al. [7]. The cube processed using the optimal parameters achieved a hardness of 480 HV, lower than the hardness of 550 HV found in as-quenched

4340 steel [23], indicating that the martensitic matrix of the as-fabricated samples was tempered during the LPBF process. Still, the relatively high hardness, comparable to wrought 4340 steel tempered at 400 °C [22], may be attributed to the fine microstructural features and high dislocation densities (10^{14} m^{-2}) [24,25] commonly found in steels processed through LPBF.

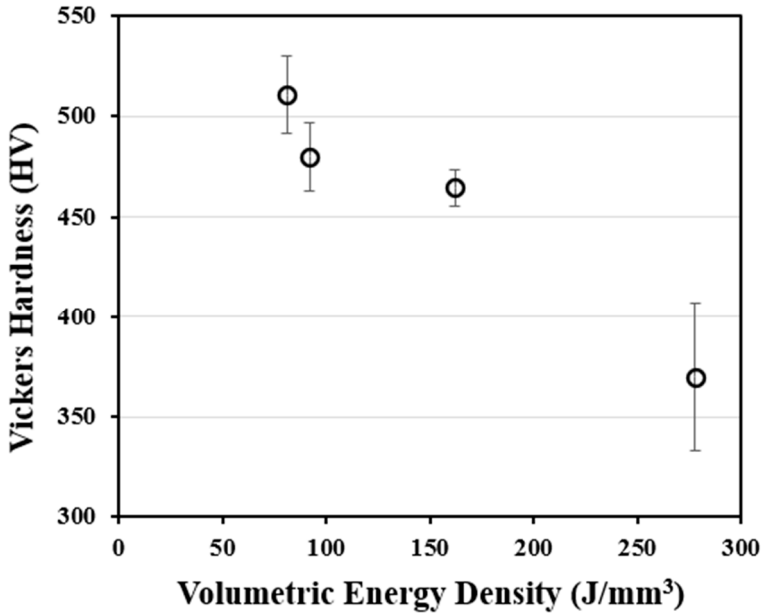

Figure 12. Vickers hardness of as-fabricated 4340 steel as a function of VED.

Figure 13 presents the Vickers hardness values across different regions of the as-fabricated 4340 steel cubes. No significant variation in hardness was observed as a function of build height for the sample built with optimal LPBF parameters in Figure 13b, which is similar to what has been reported in the literature for near dense samples [14]; a similar behavior was exhibited by the LPBF 4340 steel sample printed using 200 W, 200 mm/s. This further confirms the microstructural homogeneity observed in the as-fabricated samples. The LPBF 4340 steel sample printed using 350 W and 1200 mm/s was the only sample tested that showed increasing hardness values at higher build height. This phenomenon may be attributed to a lesser degree of tempering caused by the interference of efficient heat flow across the sample owing to the presence of lack of fusion flaws [26].

Figure 14 presents the engineering tensile stress vs. strain curves for LPBF AISI 4340 steel produced using the optimized parameters for laser power and laser scan speeds of 200 W and 600 mm/s, respectively. The average yield strength, ultimate tensile strength, modulus of elasticity, and elongation values achieved were 1317 ± 16 MPa, 1538 ± 22 MPa, 196.8 ± 5.7 GPa, and 18.6 ± 1%, respectively. These are comparable to those reported by Yao et al. [7]. The higher elongation achieved by the as-fabricated samples, which is comparable to wrought 4340 steel tempered at 650 °C, further demonstrates that the samples were exposed to in situ tempering during the LPBF process, as conventionally quenched 4340 steel have been reported to have an elongation of 4.5% [23]. Figure 15 further demonstrates the ductility of the LPBF 4340 steel, as the fracture features are characteristic of those of ductile mode failure with dimples. Moreover, the as-fabricated samples were able to achieve yield and ultimate tensile strength values, similar to those reported in the literature [12–14], which are comparable to wrought 4340 steel with martensite tempered at 400 °C [23]. This mechanical performance exhibited by the as-print sample can be attributed to the predominant tempered martensite found in the LPBF 4340 steel.

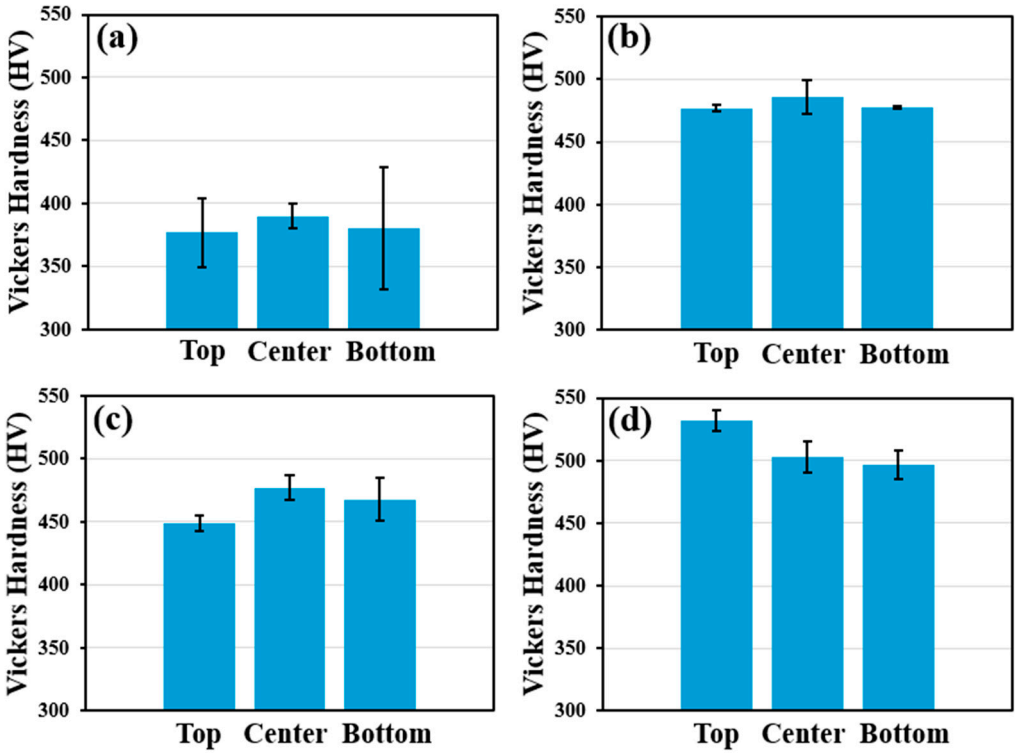

Figure 13. Vicker hardness of different regions of as-fabricated 4340 steel cubes produced using 200 W and (**a**) 200 mm/s and (**b**) 600 mm/s; and 350 W (**c**) 600 mm/s (**d**) 1200 mm/s.

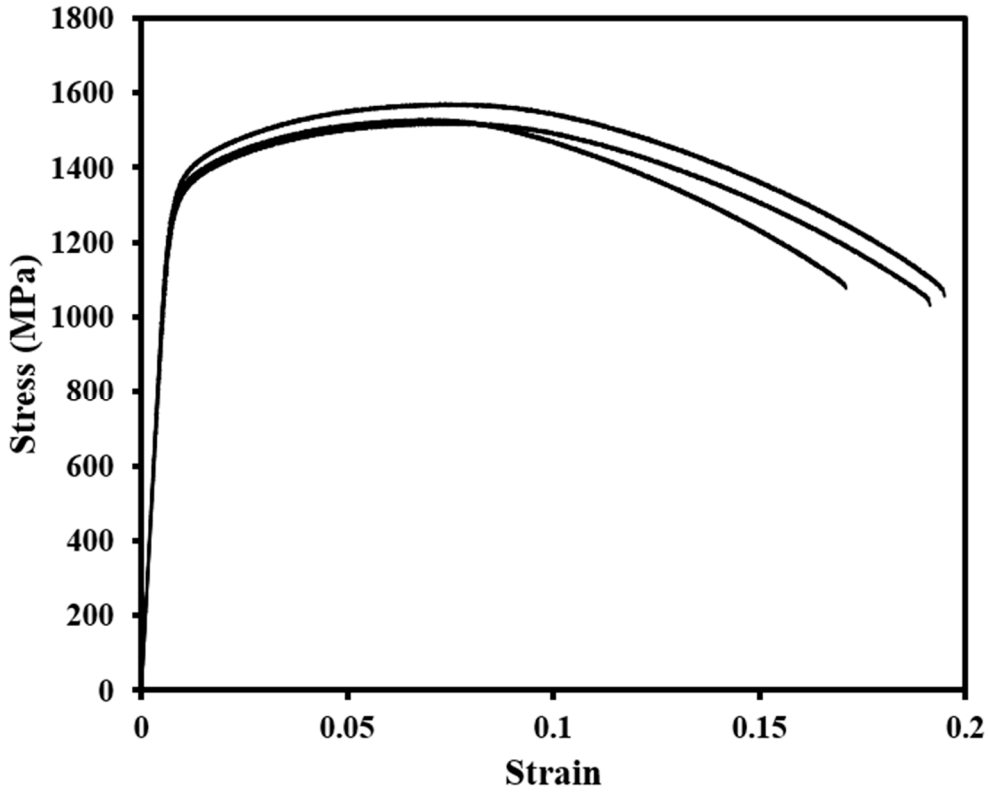

Figure 14. Engineering tensile stress–strain curves for as-fabricated AISI 4340 specimens built with laser power of 200 W and scanning speed of 600 mm/s.

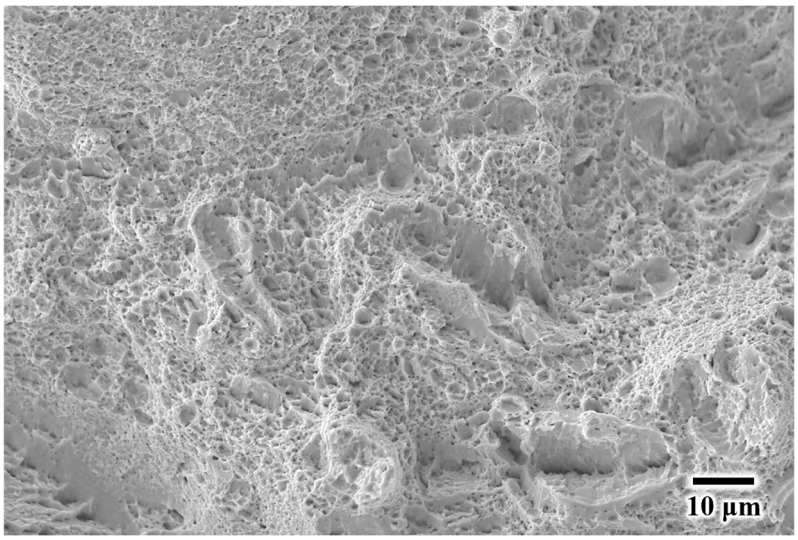

Figure 15. Secondary electron micrograph from the fracture surface of as-fabricated LPBF AISI 4340 steel.

4. Discussion

4.1. LPBF Process Influence on the Presence of Retained Austenite in As-Fabricated 4340 Steel

Factors that would influence the presence of retained austenite in the martensitic matrix of the LPBF-processed AISI 4340 steel include prior austenite grain size and solidification cell structures. It is known that a smaller prior austenite grain size lowers the M_s temperature, thus allowing for the presence of retained austenite after quenching [27]. Zuback and DebRoy [28] reported that the greater energy input in AM leads to grain size coarsening. Therefore, the prior austenite grain size in 4340 steel fused using lower VEDs would be expected to decrease, potentially leading to the appearance of increasing amounts of retained austenite in as-printed 4340 steel via the lowering of the M_s temperature.

Freeman et al. [16] also proposed that the presence of retained austenite in LPBF-processed 17-4 PH martensitic steels can be attributed to the solidification cells found in the as-print steel. The cellular structure was claimed to be robust enough to prevent the displacive phase transformation to martensite from austenite due to the presence of dense dislocation walls around the solidification cells. These cellular walls would suppress the formation of thermally induced martensite in the as-built samples, with smaller solidification cell sizes being more effective at preventing the formation of martensite.

The relationship between dendrite arm spacing and cooling rate can be expressed as follows [29,30]: $\lambda_1 = a\dot{T}^{-n}$, where λ_1 is the primary dendrite arm spacing, which in this study corresponds to the solidification cell diameter, and $\dot{T}$ is the cooling rate. The constants "a" and "n" are material-specific coefficients. Therefore, a higher cooling rate results in a smaller solidification cell size. According to Zuback and DebRoy [28], the cooling rate for LPBF decreases with increasing volumetric energy density. Therefore, at lower VEDs, the thermally induced transformation of martensite in the LPBF 4340 steel would be suppressed by the presence of smaller cell sizes. This corresponds well with the increasing fraction of retained austenite at lower VEDs, as presented in Figure 9.

4.2. LPBF Process Influence on the Hardness of As-Fabricated 4340 Steel

The factors that influence the hardness in the as-fabricated 4340 samples include the softening of the martensitic matrix induced by the effective in situ tempering, presence of porosity, and the amount of retained austenite. A reduction in hardness of the martensitic matrix with increasing VED can be explained by the LPBF in situ tempering effects on the

sample with higher VEDs. Hearn et al. [26] reported a similar behavior in LPBF 0.45C steel and attributed the decrease in hardness with increasing VED to the tempering of the martensite in the alloy during the LPBF process. Hearn et al. [26] also postulated that at lower VED, the reduced energy input for in situ tempering, combined with the presence of lack of fusion flaws can interfere with heat transfer, causing the martensite to be relatively un-tempered, yielding higher hardness. Higher VED would lead to a decrease in hardness with higher energy input and efficient heat transfer through fully dense alloy, effectively tempering and softening the martensite matrix.

The presence of retained austenite in martensitic steels is known to reduce the hardness of the alloy, as austenite is a softer FCC phase compared to martensite [31,32]. It would be expected that the as-fabricated samples with a higher volume fraction of retained austenite would exhibit lower hardness values. However, as reported in Figures 8 and 13, both the amount of retained austenite and the hardness in the as-fabricated samples decrease with increasing VED. This indicates that samples with higher fractions of retained austenite achieved higher hardness than those with lower retained austenite fractions, contrary to the known behavior of retained austenite.

Sastry et al. [33] reported that the retained austenite in 4340 steel, austenitized at 1200 °C and quenched-and-tempered, was mechanically unstable, and transformed into martensite upon deformation. Therefore, the high hardness observed in as-built 4340 steel with high retained austenite fractions could be due to the presence of mechanically unstable retained austenite, which displays low stacking fault energy and large work hardening [34]. Another potential explanation for the high hardness, despite the presence of more retained austenite, would be the microstructural refinement. Increasing the scan speed would refine the martensitic structure and increase the hardness, while the retained austenite fraction, despite the increase, would remain insufficient to impact hardness significantly.

5. Summary

The present study reports the effects of processing parameters on the printability, microstructural, and mechanical properties of AISI 4340 steel produced by LPBF. Key findings of this study are:

- Processing at volumetric energy densities lower than 92.6 J/mm^3 yielded lack-of-fusion flaws, while volumetric energy densities greater than 162 J/mm^3 yielded keyhole porosities. At intermediate volumetric energy densities between 92.6 and 162 J/mm^3, relative sample densities above 99.8% were achieved for AISI 4340 steel.
- As-fabricated AISI 4340 steel is primarily martensitic, decorated with cellular segregation. This microstructure did not vary significantly as a function of scan speeds and sample height for a given laser power.
- X-ray diffraction analysis revealed the presence of retained austenite in LPBF-processed 4340 steel. The volume fraction decreased with an increase in VED.
- Hardness measurements revealed that the martensite found in as-fabricated 4340 steel samples was softened due to exposure to in situ tempering during the LPBF process. The degree of in situ tempering experienced by a sample increased with increasing VED, causing samples printed with high VED to exhibit lower hardness compared to samples processed using low VED. Hardness values of LPBF 4340 steel produced using the optimized parameter set were relatively high compared to conventional quenching and 400 °C tempering heat treatment, despite the presence of retained austenite.
- Tensile testing of as-fabricated 4340 steel tensile bars displayed yield and ultimate tensile strengths of up to 1.3 GPa and 1.5 GPa, respectively, with elongations of up to 18.6%.

Author Contributions: Conceptualization, Y.S. and M.K.; methodology, Y.S. and T.H.; validation, T.H. and N.K.; formal analysis, F.A. and N.K.; investigation, F.A. and N.K.; resources, Y.S. and M.K.; data curation, F.A. and T.H.; writing—original draft preparation, F.A.; writing—review and editing, Y.S.; visualization, F.A. and Y.S.; supervision, Y.S. and M.K. All authors have read and agreed to the published version of the manuscript.

Funding: This research received no external funding.

Data Availability Statement: The raw data supporting the conclusions of this article will be made available by the authors on request.

Conflicts of Interest: The authors declare no conflicts of interest.

References

1. Herzog, D.; Seyda, V.; Wycisk, E.; Emmelmann, C. Additive manufacturing of metals. *Acta Mater.* **2016**, *117*, 371–392.
2. DebRoy, T.; Wei, H.L.; Zuback, J.S.; Mukherjee, T.; Elmer, J.W.; Milewski, J.O.; Beese, A.M.; Wilson-Heid, A.; De, A.; Zhang, W. Additive manufacturing of metallic components–process, structure and properties. *Prog. Mater. Sci.* **2018**, *92*, 112–224.
3. Sames, W.J.; List, F.A.; Pannala, S.; Dehoff, R.R.; Babu, S.S. The metallurgy and processing science of metal additive manufacturing. *Int. Mater. Rev.* **2016**, *61*, 315–360.
4. de Souza, M.F.; Serrão, L.F.; Pardal, J.M.; Tavares, S.S.M.; Fonseca, M.C. Tempering influence on residual stresses and mechanical properties of AISI 4340 Steel. *Int. J. Adv. Manuf. Technol.* **2022**, *120*, 1123–1134.
5. Jelis, E.; Clemente, M.; Hespos, M.; Groeschler, S.; Golden, E.; Carpenter, R. Round Robin study evaluating consistency of 4340 steel specimens manufactured by different laser powder bed fusion machines. *J. Mater. Eng. Perform.* **2021**, *30*, 6832–6843. [CrossRef]
6. Lim, N.S.; Bang, C.W.; Das, S.; Jin, H.W.; Ayer, R.; Park, C.G. Influence of tempering temperature on both the microstructural evolution and elemental distribution in AISI 4340 Steels. *Met. Mater. Int.* **2012**, *18*, 87–94. [CrossRef]
7. Yao, J.; Tan, Q.; Venezuela, J.; Atrens, A.; Zhang, M.X. Additive manufacturing of high-strength low-alloy AISI 4340 steel with an optimal strength-ductility-toughness trade-off. *Addit. Manuf.* **2024**, *94*, 104496.
8. McDaniels, R.L.; White, S.A.; Liaw, K.; Chen, L.; McCay, M.H.; Liaw, P.H. Effects of a laser surface processing induced heat-affected zone on the fatigue behavior of AISI 4340 steel. *Mater. Sci. Eng. A* **2008**, *485*, 500–507. [CrossRef]
9. Keshavarzkermani, A.; Marzbanrad, E.; Esmaeilizadeh, R.; Mahmoodkhani, Y.; Ali, U.; Enrique, P.D.; Zhou, N.Y.; Bonakdar, A.; Toyserkani, E. An investigation into the effect of process parameters on melt pool geometry, cell spacing, and grain refinement during laser powder bed fusion. *Opt. Laser Technol.* **2019**, *116*, 83–91.
10. Mishutova, T.; Artzt, K.; Haubrich, J.; Requena, G.; Bruno, G. New aspects about the search for the most relevant parameters optimizing SLM materials. *Addit. Manuf.* **2019**, *25*, 325–334.
11. Cherry, J.A.; Davies, H.M.; Mehmood, S.; Lavery, N.P.; Brown, S.G.R.; Sienz, J. Investigation into the effect of process parameters on microstructural and physical properties of 316L stainless steel parts by selective laser melting. *Int. J. Adv. Manuf. Technol.* **2015**, *76*, 869–879. [CrossRef]
12. Ryder, M.A.; Montgomery, C.J.; Brand, M.J.; Carpenter, J.S.; Jones, P.E.; Spangenberger, A.G.; Lados, D.A. Melt Pool and Heat Treatment Optimization for the Fabrication of High-Strength and High-Toughness Additively Manufactured 4340 Steel. *J. Mater. Eng. Perform.* **2021**, *30*, 5426–5440. [CrossRef]
13. Hearn, W.; Harlin, P.; Hryha, E. Development of powder bed fusion–laser beam process for AISI 4140, 4340 and 8620 low-alloy steel. *Powder Metal.* **2023**, *66*, 94–106. [CrossRef]
14. Jelis, E.; Hespos, M.R.; Ravindra, N.M. Process Evaluation of AISI 4340 Steel Manufactured by Laser Powder Bed Fusion. *J. Mater. Eng. Perform.* **2018**, *27*, 63–71. [CrossRef]
15. *E8/E8M-24*; Standard Test Methods for Tension Testing of Metallic Materials. ASTM International: West Conshohocken, PA, USA, 2024.
16. Sastry, C.N.; Wood, W.E. On the presence of retained austenite at the prior austenite grain boundaries of AISI 4340 steel. *Mater. Sci. Eng.* **1980**, *45*, 277–280. [CrossRef]
17. Freeman, F.S.H.B.; Sharp, J.; Xi, J.; Todd, I. Influence of solidification cell structure on the martensitic transformation in additively manufactured steels. *Addit. Manuf.* **2019**, *30*, 100917. [CrossRef]
18. Fastow, M.; Bamberger, M.; Nir, N.; Landkof, M. Laser surface melting of AISI 4340 steel. *Mater. Sci. Technol.* **1990**, *6*, 900–904. [CrossRef]
19. Lee, Y.K.; Shin, H.C.; Leem, D.S.; Choi, J.K.; Jin, W.; Choi, C.S. Reverse transformation mechanism of martensite to austenite and amount of retained austenite after reverse transformation in Fe-3Si-13Cr-7Ni (wt-%) martensitic stainless steel. *Mater. Sci. Tech.* **2013**, *19*, 393–398. [CrossRef]

20. Chou, C.Y.; Petterson, N.H.; Durga, A.; Zhang, F.; Oikonomou, C.; Borgenstam, A.; Odqvist, J.; Lindwall, G. Influence of solidification structure on austenite to martensite transformation in additively manufactured hot-work tool steels. *Acta Mater.* **2021**, *215*, 117044. [CrossRef]
21. Seede, R.; Shoukr, D.; Zhang, B.; Whitt, A.; Gibbons, S.; Flater, P.; Elwany, A.; Arroyave, R.; Karaman, I. An ultra-high strength martensitic steel fabricated using selective laser melting additive manufacturing: Densification, microstructure, and mechanical properties. *Acta Mater.* **2020**, *186*, 199–214. [CrossRef]
22. Seede, R.; Zhang, B.; Whitt, A.; Picak, S.; Gibbons, S.; Flater, P.; Elwany, A.; Arroyave, R.; Karaman, I. Effect of heat treatments on the microstructure and mechanical properties of an ultra-high strength martensitic steel fabricated via laser powder bed fusion additive manufacturing. *Addit. Manuf.* **2021**, *47*, 102255.
23. Lee, W.; Su, T. Mechanical properties and microstructural features of AISI 4340 high-strength alloy steel under quenched and tempered conditions. *J. Mater. Process. Technol.* **1999**, *87*, 198–206.
24. Pokharel, R.; Balogh, L.; Brown, D.W.; Clausen, B.; Grayz, G.T., III; Livescu, V.; Vogel, S.C.; Takajo, S. Signatures of the unique microstructure of additively manufactured steel observed via diffraction. *Scr. Mater.* **2018**, *155*, 16–20.
25. Wu, L.; Khan, D.F.; Zhang, C.; Zhang, R.; Jiang, X.; Wang, Y.; Liu, G.; Yin, H.; Su, J.; Qu, X. Microstructure and mechanical characterization of additively manufactured $Fe_{11}Cr_8Ni_5Co_3Mo$ martensitic stainless steel. *Mater. Charact.* **2023**, *203*, 113106. [CrossRef]
26. Hearn, W.; Lindgren, K.; Persson, J.; Hryha, E. In situ tempering of martensite during laser powder bed fusion of Fe-0.45C steel. *Materialia* **2022**, *23*, 101459.
27. Yang, H.; Bhadeshia, H.K.D.H. Austenite grain size and the martensite-start temperature. *Scr. Mater.* **2009**, *60*, 493–495.
28. Zuback, J.S.; DebRoy, T. The Hardness of Additively Manufactured Alloys. *Materials* **2018**, *11*, 2070. [CrossRef]
29. Flemings, M.C. Solidification Processing. *Metal. Trans.* **1974**, *5*, 2121–2134.
30. Gilath, I.; Signamarcheix, J.M.; Bensussan, P. A comparison of methods for estimating the weld-metal cooling rate in laser welds. *J. Mater. Sci.* **2004**, *29*, 3358–3362. [CrossRef]
31. Park, J.; Jeon, J.; Seo, N.; Kang, S.; Son, S.B.; Lee, S.; Jung, J. Microstructure and mechanical behavior of AISI 4340 steel fabricated via spark plasma sintering and post-heat treatment. *Mater. Sci. Eng. A* **2023**, *862*, 144433.
32. Galindo-Nava, E.I.; Rivera-Díaz-del-Castillo, P.E.J. Understanding the factors controlling the hardness in martensitic steels. *Scr. Mater.* **2016**, *110*, 96–100. [CrossRef]
33. Sastry, C.N.; Khan, K.H.; Wood, W.E. Mechanical Stability of Retained Austenite in Quenched and Tempered AISI 4340 Steel. *Metall. Trans. A* **1982**, *13*, 676–680. [CrossRef]
34. Mola, J.; Seo, E.J.; Cho, L. Correlation between mechanical stability and hardness of austenite in martensite/austenite mixtures. *Mater. Sci. Eng. A* **2021**, *822*, 141687.